ACS APPLIED MATERIALS & INTERFACES

Research Article

www.acsami.org

Hollow Nanobarrels of α-Fe_2O_3 on Reduced Graphene Oxide as High-Performance Anode for Lithium-Ion Batteries

Kang Soo Lee,[†,‡] Seyong Park,[‡] Wooyoung Lee,[*,†] and Young Soo Yoon[*,‡]

[†]Department of Materials Science and Engineering, Yonsei University, Shinchondong, 262 Seongsanno, Seodaemoongu, Seoul 120-749, Republic of Korea

[‡]Department of Environment and Energy Engineeering, Gachon University, Seongnamdaero 1342, 461-710 Gyeonggi-do, Seongnam, Republic of Korea

Supporting Information

ABSTRACT: Alpha-phase iron oxide nanoparticles (α-NPs), α-iron oxide hollow nanobarrels (α-HNBs), and α-HNBs on reduced graphene oxide (α-HNBs/RGO) for Li-ion batteries (LIBs) were synthesized by a time-efficient microwave method to improve the low electrical conductivity of iron oxide and exploit the porous structure of RGO, which prevents the volume expansion of α-Fe_2O_3 during the insertion/extraction. On the other hand, α-HNBs (~200 nm in diameter, ~360 nm in length) provide a short diffusion path for Li ions and accommodate the strain generated by the volume change. The α-HNBs/RGO hybrid structure was synthesized by a one-step microwave-assisted hydrothermal method to bond α-HNBs with RGO. The as-prepared α-HNBs/RGO electrode exhibited a superior reversible capacity of 1279 mA h g^{-1} at 0.5 C after the first cycle; such a capacity was nearly recovered after numerous cycles (2nd to 100th cycle, 95%). The long-term cyclability of α-HNBs/RGO shows 478 mA h g^{-1} after 1000 cycles. Moreover, the α-HNBs/RGO electrode shows a high rate capacity of 403 mA h g^{-1} even at 10 C. The α-HNBs/RGO exhibited a better electrochemical performance that could be attributed to the absence of nanoparticle agglomeration and RGO restacking, which provided a buffer effect against the volume expansion, promoted electrical conductivity and high structural integrity.

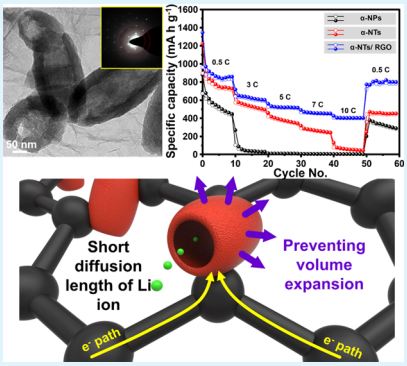

KEYWORDS: *iron oxide, reduced graphene oxide, high rate performance, anode, lithium-ion batteries*

1. INTRODUCTION

The development of promising eco-friendly anode materials for Li-ion batteries (LIBs) with high capacity, rate capability, and cyclability is necessary for portable devices, hybrids, plug-in hybrids, and electric vehicles.[1−6] Recently, various types of graphite have been used as anode materials because of their relatively low potential, stable cycle performance, low cost, and nontoxicity. However, graphite has a theoretical capacity of only 372 mA h g^{-1}, which is insufficient to meet the high capacity demand of LIBs.[7,8] Thus, various metal oxides (MOx; M: Ti, Sn, Fe, Co, Cu, Ni, V, etc.)[9−19] have been widely developed to achieve a better LIB performance than that of commercial electrodes, as metal oxides have a high energy density of Li ions. To this end, Fe_2O_3 as an anode material for LIBs has been considered due to its low cost, nontoxicity, natural abundance, and large theoretical reversible capacity (~1007 mA h g^{-1}) based on a maximum accommodation of 6Li/Fe_2O_3.[20,21] In particular, the electrical conductivity of Fe_2O_3 ($s \sim 2 \times 10^4$ S m^{-1}) is higher than that of most metal oxides.[22] However, Fe_2O_3 also exhibits a significant volume change during the Li-ion insertion/extraction reaction, which induces the delamination of the active materials from the current collector, causing the breakdown of the electrical connection, a large irreversible capacity, poor electrochemical cyclability, and low rate capability.[23] These problems cannot be overcome by simply reducing the particle size to nanoscale.[23,24] Recently, many alternatives, including nanorods, passivation coatings, and composites with conductive materials, have been considered to enhance the cyclability and rate capability of Fe_2O_3.[25−27] Up to now, various studies of iron oxide/carbon composites have been carried out for anodes, such as Fe_2O_3 nanoparticles wrapped in multiwalled carbon nanotubes,[28] Fe_2O_3 nanotube/RGO composite,[29] Fe_2O_3 nanorods,[25] Fe_2O_3 rice on graphene,[27] and nanosized Fe_2O_3 decorated single-walled carbon nanotube.[30] It has been seen that these carbon content not only the electrical conductivity of iron oxide but also buffer effect of volume expansion. However, it is still unsuitable to meet the required high rate capability and clear the long-term cycle test. Thus, in this study, the synergetic effect of alpha-phase iron oxide nanobarrels on reduced graphene oxide (α-HNBs/RGO) is exploited to maximize the practical use of RGO and α-Fe_2O_3 as anode materials and improve the electrochemical performance, resistance to volume expansion, and electrical conductivity of Fe_2O_3. The use of RGO as a conductive material with metal oxides has been widely successful for various reasons: (1) good electrical

Received: October 28, 2015
Accepted: December 30, 2015
Published: December 30, 2015

DOI: 10.1021/acsami.5b10342
ACS Appl. Mater. Interfaces 2016, 8, 2027−2034

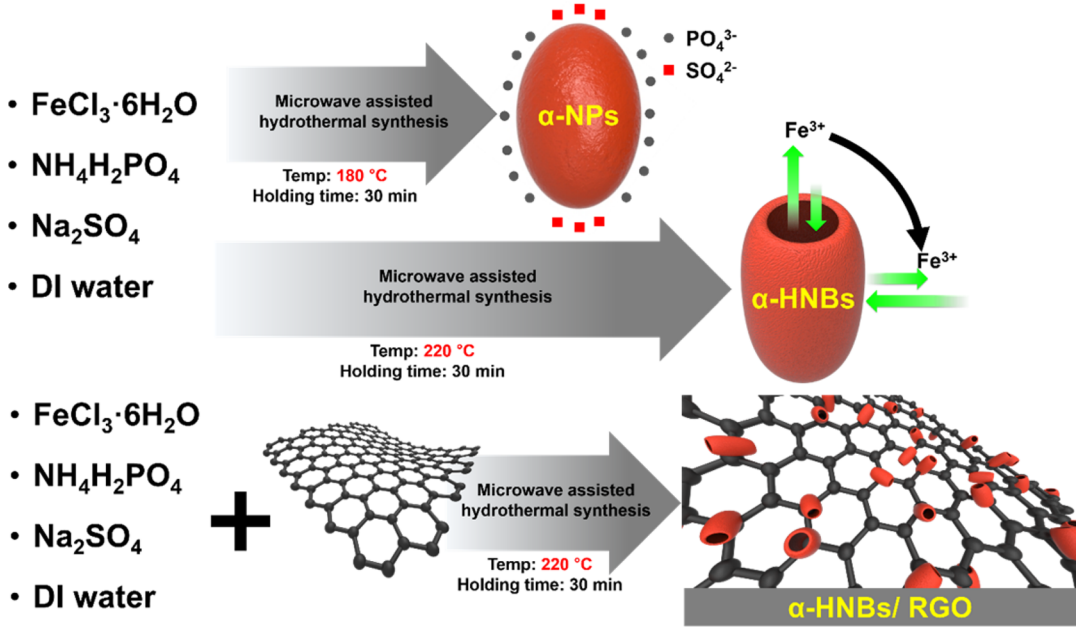

Figure 1. Schematic of the preparation process of double-anion-assisted synthesis of α-NPs, α-HNBs, and α-HNBs/RGO.

conductivity; (2) high specific surface area, ~1000 m^2 g^{-1}; (3) high surface-to-volume ratio, which can accommodate many reaction sites for the electrochemical reaction of the Li ions; (4) use in harsh environments because of its high chemical stability; and (5) the presence of numerous functional groups, which deliver functional materials, such as active materials for LIBs, to bonding sites.[31,32] The α-HNBs, which are used to provide a higher resistance to the volume expansion than other types of nanostructures and a short path for the diffusion of the Li ions (wall thickness of ~20 nm), were synthesized by a one-step microwave-assisted hydrothermal process. It can be a time-efficient process than the hydrothermal process. Even though the hydrothermal process has many advantages, one of the drawbacks is the long-term synthesis process. By contrast, the microwave-assisted hydrothermal process gives a shorter reaction time to produce similar results of the experiment.

The substantial synergistic effects of α-HNBs/RGO depend on the shape effects of Fe_2O_3 and interfacial interactions, which can be summarized as follows: (1) RGO acts as a support for the homogeneous anchoring or good dispersion of Fe_2O_3; (2) Fe_2O_3 obstructs the restacking of the RGO layers; (3) RGO acts as a conductive layer to enhance the high electrochemical activity of Fe_2O_3; (4) a three-dimensional porous template of RGO and α-HNBs is formed, which prevents volume expansion; and (5) functional groups are present on RGO, which provide good bonding, interfacial reaction, and electrical contact between RGO and α-HNBs. As a result, the synergistic effect between RGO and α-HNBs could reduce the initial capacity loss as well as improve the high rate capability (10 C) and cyclablility (1000 cycles).

2. EXPERIMENTAL SECTION

2.1. Material Preparation. The α-NPs, α-HNBs, and α-HNBs/RGO were synthesized via a microwave-assisted hydrothermal process (MARS 6, CEM Co.). The α-NPs and α-HNBs precursors were synthesized by a double-anion-assisted hydrothermal method reported by Jia et al.[33] First, 338 mg of $FeCl_3·6H_2O$, 2.7 mg of $NH_4H_2PO_4$, and 28.5 mg of Na_2SO_4 were stirred for 2 h in 40 mL of deionized (DI) water. Subsequently, the solution was transferred to a Teflon-lined microwave vessel and heated at 180 °C (α-NPs) and 220 °C (α-HNBs) for 30 min. After cooling the vessel to room temperature, the red precipitate was collected by centrifugation, washed with DI water, and dried in a vacuum oven at 80 °C for 8 h.

In addition, a one-step microwave-assisted hydrothermal synthesis at 220 °C for 30 min was concurrently conducted with 20 mg of RGO (Graphene supermarket), 338 mg of $FeCl_3·6H_2O$, 2.7 mg of $NH_4H_2PO_4$, and 28.5 mg of Na_2SO_4 in 40 mL of DI water to obtain a more homogeneous dispersion and chemical bonding (Figure 1) than those obtained with the separate synthesis (Figure S1), which was conducted with 60 mg of presynthesized α-HNBs and 20 mg of RGO at 220 °C for 30 min.

In the case of one-step synthesis of α-HNBs with RGO, the anchoring effect of α-HNBs can be confirmed by the dark red precipitation (Figure S2a), which is not observed in the two-step synthesis process. The two-step synthesis process of α-HNBs and RGO shows dispersed red color of α-HNBs in DI water. It is due to no strong bond formation in this process, as shown in Figure S2b. Subsequently, the specimens were annealed in a furnace at 300 °C to remove the adsorbed water molecules under a vacuum of 6.6 Pa in a N_2 atmosphere.

2.2. Material Characterization. The morphologies and microstructures of α-NPs, α-HNBs, and α-HNBs/RGO were characterized by field emission scanning electron microscopy (FE-SEM) using a Hitachi S-4200 system, and high-resolution transmission electron microscopy (HR-TEM) using a JEM-2100F, JEOL microscope. The crystal structures of the specimens were examined by X-ray diffraction (XRD, Rigaku RINT) using Cu−Kα radiation with λ = 1.5418 Å. Thermal gravimetric analysis (TGA) using a SDT Q600 V20.9 Build 20 (TA Instruments) system was performed under both air and nitrogen atmospheres with a ramp rate of 10 °C min^{-1} from 25 to 800 °C. Nitrogen adsorption isotherms and Brunauer, Emmett, and Teller (BET) surface area were measured by a Micromeritcs ASAP 2020 analyzer. X-ray photoelectron spectroscopy (XPS) (Thermo VG, U.K.) using a monochromated Al X-ray source (Al−Kα line: 1486.6 eV) was conducted to analyze the bonding state and elemental distribution. The α-HNBs/RGO was characterized by a LabRAM ARAMIS Raman spectrometer (LabRAM HORIBA Jobin Yvon, Edison, NJ) with excitation source of an Ar laser (λ = 514.532 nm, 0.5 mW).

2.3. Electrochemical Characterization. To evaluate the electrochemical performance, α-NPs, α-HNBs, and α-HNBs/RGO were used to prepare the active material (70 wt %) along with polyvinylidene

DOI: 10.1021/acsami.5b10342
ACS Appl. Mater. Interfaces 2016, 8, 2027−2034

fluoride as the binder (20 wt %) and conductive carbon black (10 wt %) with 1-methyl-2-pyrrolidinone. The slurry was deposited on a 20 μm thick Cu foil using an omatic doctor blade apparatus, and then dried under vacuum at 80 °C for 12 h. Subsequently, the as-prepared sheets were punched to form disk-type electrodes. All the electrochemical measurements were performed with a coin cell (CR2032) for the half-cell test, which was assembled in an argon-filled glovebox using Li foil (0.5 mm thick) as the counter electrode and 1 M $LiPF_6$ in EC:DEC (1:1) as the electrolyte. All the coin cells were cycled by a battery cycler (WBCS3000) at room temperature (~298 K) with a cutoff voltage between 0.01 and 3 V. Electrochemical impedance spectroscopy analyses (BioLogic EC-Lab, VSP-300) were conducted in the frequency range between 4 MHz and 100 mHz before the cycling test.

3. RESULTS AND DISCUSSION

3.1. Material Characterization. The XRD patterns of α-NPs, α-HNBs, and α-HNBs/RGO are shown in Figure 2; all

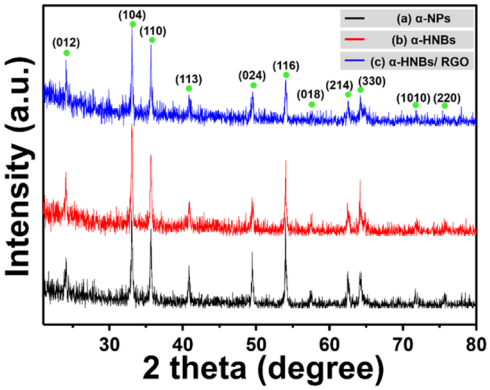

Figure 2. X-ray diffraction patterns of (a) alpha-phase iron oxide nanoparticles (α-NPs), (b) nanobarrels (α-HNBs), and (c) α-HNBs on reduced graphene.

the diffraction peaks are well indexed to those of α-Fe_2O_3 (JCPDS, 330664). The sharp diffraction peaks clearly indicate the good crystallinity of the α-Fe_2O_3 phase. Moreover, no noticeable diffraction peaks of graphite were observed that the RGO sheets are gradually decreased in crystallinity according to the increasing reduction times, which means a fully reduced oxygen group.[34] These results confirm that the α-NPs, α-HNBs, and α-HNBs/RGO have an identical crystal structure.

The TEM images (Figure 3) show the morphology of the α-NPs, α-HNBs, and α-HNBs/RGO. The anchoring of the α-HNBs on the RGO sheets was clearly observed by TEM and HRTEM, as shown in Figure 3e,f. Tubular and short α-HNBs with a length of ~360 nm and outer diameter of ~200 nm appear homogeneously dispersed on the RGO sheets. The integration of the α-HNBs in the RGO sheets promoted the electron transfer during the insertion/extraction process. The α-HNBs (Figure 3c) were successfully formed by using the $NH_4H_2PO_4$ and Na_2SO_4 powders as surfactants during the microwave-assisted hydrothermal process and can be clearly distinguished from the α-NPs shown in Figure 3a. According to the XRD results, the periodic lattice fringes of the α-NPs and α-HNBs shown in the HRTEM images (Figure 3b,d) were oriented along the (012) and (104) planes. The insets of Figure 3b,d,f show the selected-area electron diffraction (SAED) patterns of each specimen, revealing the diffraction plane. The SAED pattern of α-HNBs/RGO (Figure 3f) showed not only the diffraction spots of the α-HNBs but also the ring pattern

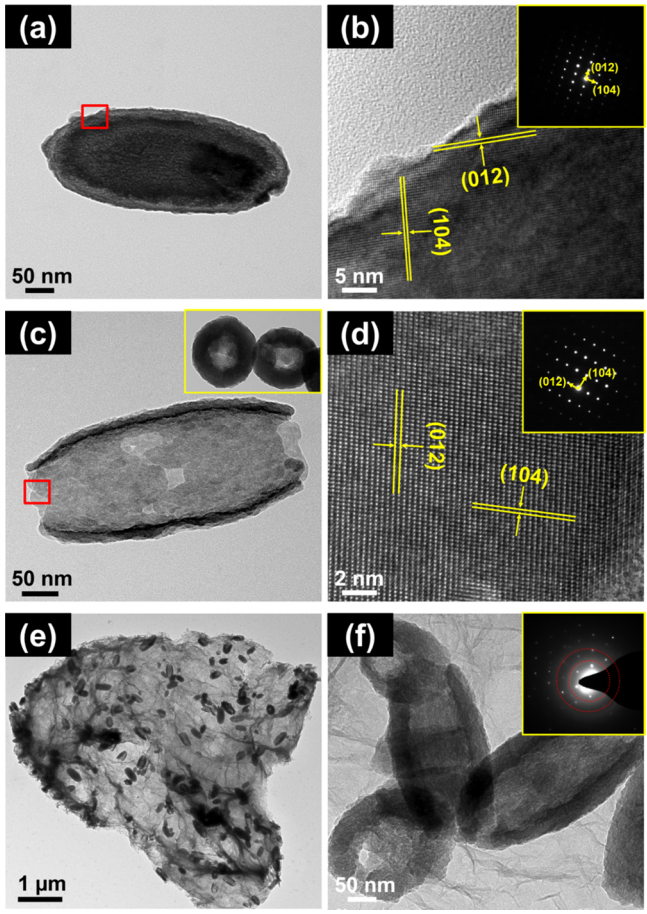

Figure 3. Transmission electron microscopy images of (a) α-NPs, (c) α-HNBs (inset top view of the α-HNBs), and (e) α-HNBs on reduced graphene (α-HNBs/RGO). High-resolution images of (b) α-NPs with selected-area electron diffraction (SAED) pattern (inset), (d) α-HNBs with SAED pattern (inset), and (f) α-HNBs/RGO with SAED pattern (inset).

and simple hexagonal pattern with sharp spots of RGO, which can be attributed to the presence of three to five layers and a crystalline structure, respectively.[11,35] Here, the presence of the RGO sheets in the solution might act as a heterogeneous nucleation site to enable the formation of anchoring α-HNBs, which has not been reported for LIBs.

Meanwhile, the TEM image (Figure S1) of the separated synthesized α-HNBs/RGO specimen shows a small amount of α-HNBs, poor distribution of α-HNBs on RGO, and unanchored α-HNBs. From these results, the α-HNBs/RGO composite exhibits a larger loading amount of α-HNBs, a homogeneous distribution, and good contact with RGO. The unique structural features deriving from the anchoring of the α-HNBs on the RGO sheets were expected to accommodate the large volume expansion of α-Fe_2O_3 owing to the free space resulting from the insertion/extraction, as well as control the short diffusion length of the Li^+ ions.[36−38]

The α-HNBs/RGO composite was evaluated by TGA analysis to define the weight ratio (wt %) of the RGO and α-Fe_2O_3 components. The TGA results of bare RGO in air, bare RGO in a N_2 atmosphere, and α-HNBs/RGO in air are shown in Figure S4a−c. From these results, an annealing temperature of 300 °C was confirmed below the decomposition temperature of RGO in the N_2 atmosphere, as in the N_2 atmosphere a limited decomposition of RGO is shown (Figure S4b). The ~1

DOI: 10.1021/acsami.5b10342
ACS Appl. Mater. Interfaces 2016, 8, 2027−2034

wt % loss near 250 °C corresponded to the desorption of adsorbed H_2O molecules. The decomposition of the RGO in α-HNBs/RGO occurs up to 593 °C, resulting in ∼48 wt %. Thus, the weight percent of α-HNBs/RGO revealed the presence of RGO (∼48 wt %) and α-Fe_2O_3 (∼52 wt %).

The surface areas of α-NPs, α-HNBs, and α-HNBs/RGO were investigated by nitrogen adsorption/desorption isotherms, as shown in Figure S5. The BET specific areas were 16 m^2 g^{-1} for α-NPs, 21 m^2 g^{-1} for α-HNBs, and 87 m^2 g^{-1} for α-HNBs/RGO. While the surface areas of α-NPs and α-HNBs were similar, the α-HNBs/RGO specimens exhibited a considerably higher specific area, which may promote the storage of Li.

To confirm the chemical bonding state of α-HNBs/RGO, XPS analysis was conducted, as shown in Figure 4. In the O 1s

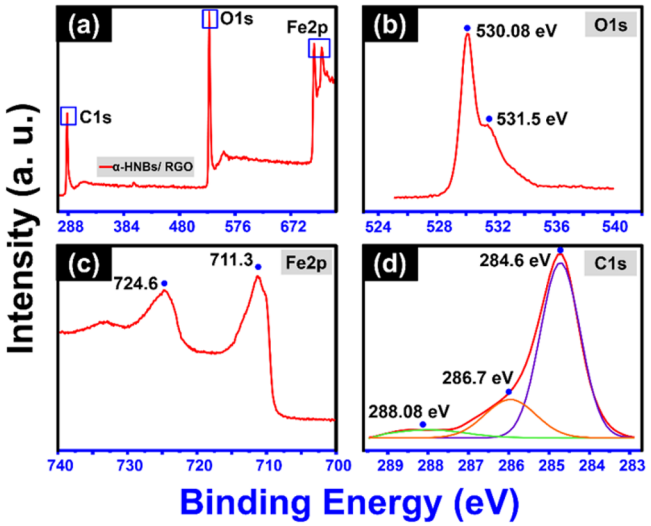

Figure 4. X-ray photoelectron spectroscopy spectra: (a) wide scan of α-HNBs/RGO and narrow scan of (b) O 1s, (c) Fe 2p, and (d) C 1s spectra.

spectrum (see Figure 4b), the peaks at 530.08 and 531.5 eV were assigned to O^{2-} and C−O bonding.[39] On the other hand, the peaks at 531.5 and 533 eV belonging to H_2O and OH−, respectively, were not observed in the O 1s spectrum, which indicates the absence of FeOOH in the α-HNBs/RGO, as revealed by the XRD results.[26,39] The peaks at 711.3 and 724.6 eV in the Fe 2p spectrum (Figure 4c) belong to Fe $2p_{1/2}$ and Fe $2p_{3/2}$, respectively.[39,40] The C 1s spectrum revealed the presence of the C−C, C−O, and C═O bonds at 284.6, 286.7, and 288.08 eV, respectively. The spectrum of α-HNBs/RGO shows a major peak relative to the sp^2 C−C bond, which suggests the reduction of the oxygen functionalized groups.[41]

Raman spectroscopy was performed on α-HNBs/RGO to investigate the possible interaction between α-Fe_2O_3 and RGO. The α-Fe_2O_3 of α-HNBs/RGO has A_{1g} modes (221 and 499 cm^{-1}) and E_g modes (292, 409, and 614 cm^{-1}), as shown in Figure S6.[42] Moreover, the peak at ∼1599 cm^{-1} displayed the pairs of sp^2 atoms (G band).[19] The peak at ∼1330 cm^{-1} is associated with disorder (D band) in carbon sp^2. The intensity ratio ($r = I_D/I_G$) for α-HNBs/RGO (r = 1.10) shows an enhanced D band, indicating the presence of localized sp^3 defects which can offer heterogeneous nucleation sites of α-HNBs.

3.2. Electrochemical Properties. The cycling performances of the as-prepared α-NPs, α-HNBs, and α-HNBs/RGO during insertion/extraction were evaluated at 0.5 C (500 mA g^{-1}) in the cutoff voltage range of 0.01−3.0 V, as shown in Figure 5. At the first cycle, the specific capacity of the α-NPs specimen was ∼1086 mA h g^{-1}, which is near the theoretical capacity generally expected for NPs. However, the initial capacity continuously decreased to 125 mA h g^{-1} (capacity retention of ∼16% compared to the initial capacity at the 2nd cycle), as shown in Table S1, after the 100th cycle, indicating that the NPs anode still had an insufficient performance and unstable cycle retention due to the volume changes and serious aggregation of iron oxide during the insertion/extraction of the Li^+ ions.[43] The α-HNBs showed an improved capacity retention of 1153 mA h g^{-1} at the first cycle (2nd to 100th cycle ∼ 41%), as shown in Table S1, in comparison with α-NPs even similar discharge capacity. This result may be due to the structural effect provided by the α-HNBs, which can offer superior resistance to the volume expansion. In the case of the α-HNBs/RGO hybrid structure, the first cycle capacity was 1276 mA h g^{-1}, the capacity after the 100th cycle was 916 mA h g^{-1}, and the corresponding excellent capacity retention reached 95% (see Table S1) between the initial capacity and the 100th cycle. In Figure 5b, the graph showing the potential vs specific capacity of α-HNBs/RGO as the anode reveals a good reversible reaction between the 2nd and the 100th cycle. The increase of capacity retention of α-HNBs/RGO with increasing cycle number is due to a phenomenon previously reported for metal oxides/graphene composites.[44,45] It can be expected that a new surface arises during the cycling test. The Coulombic efficiency (Figure 5c) of α-NPs, α-HNBs, and α-HNBs/RGO at the first cycle was 80, 75, and 68%, respectively, which can be attributed to the irreversible reaction of the electrolyte decomposition and covering of the solid electrolyte interface (SEI) layer on the electrode.[30,46] Moreover, α-HNBs/RGO exhibited a better Coulombic efficiency than the other specimens (α-NPs: 82%; α-HNBs: 96%) with a value above 98% after the 100th cycle, and the Coulombic efficiency gradually increased to 97% after nine cycles under 500 mA g^{-1}. On the basis of these results, the long-term cycling performance of the α-HNBs/RGO at a high rate of 5 C (5 A g^{-1}) is shown in Figure 5e. The reversible specific capacity of α-HNBs/RGO was still maintained at ∼478 mA h g^{-1} after 1000 cycles. Therefore, α-HNBs as an active material maintain their structural integrity against the volume expansion during the insertion/extraction process; besides, the electrical contact between α-HNBs and RGO with the current collector is preserved.

The superior cyclic retention and high capacity of α-HNBs/RGO originated from the synergistic effect of RGO and α-Fe_2O_3. It can be explained by the following properties: good electrical conductivity induced by α-HNBs anchored on RGO; stable electrochemical characteristics deriving from a homogeneous dispersion of α-HNBs; and a unique α-HNBs structure and RGO 3D porous template, which hinder the volume expansion. Moreover, the functional groups of the RGO sheets promoted the high Li storage capacity.[47]

To compare the nobility of α-HNBs/RGO of electrochemical characteristics, the rate capabilities of α-NPs, α-HNBs, and α-HNBs/RGO as anodes were examined at the various current densities of 0.5, 1, 2.5, 4, 5, and 0.5 C (Figure S7 and Table S2). Moreover, α-NPs, α-HNBs, and α-HNBs/RGO were examined at high current densities of 0.5, 3, 5, 7, and 10 C, as shown in Figure 5d. The α-NPs electrode exhibited the lowest rate capability, significantly decreasing from 445 mA h

DOI: 10.1021/acsami.5b10342
ACS Appl. Mater. Interfaces 2016, 8, 2027−2034

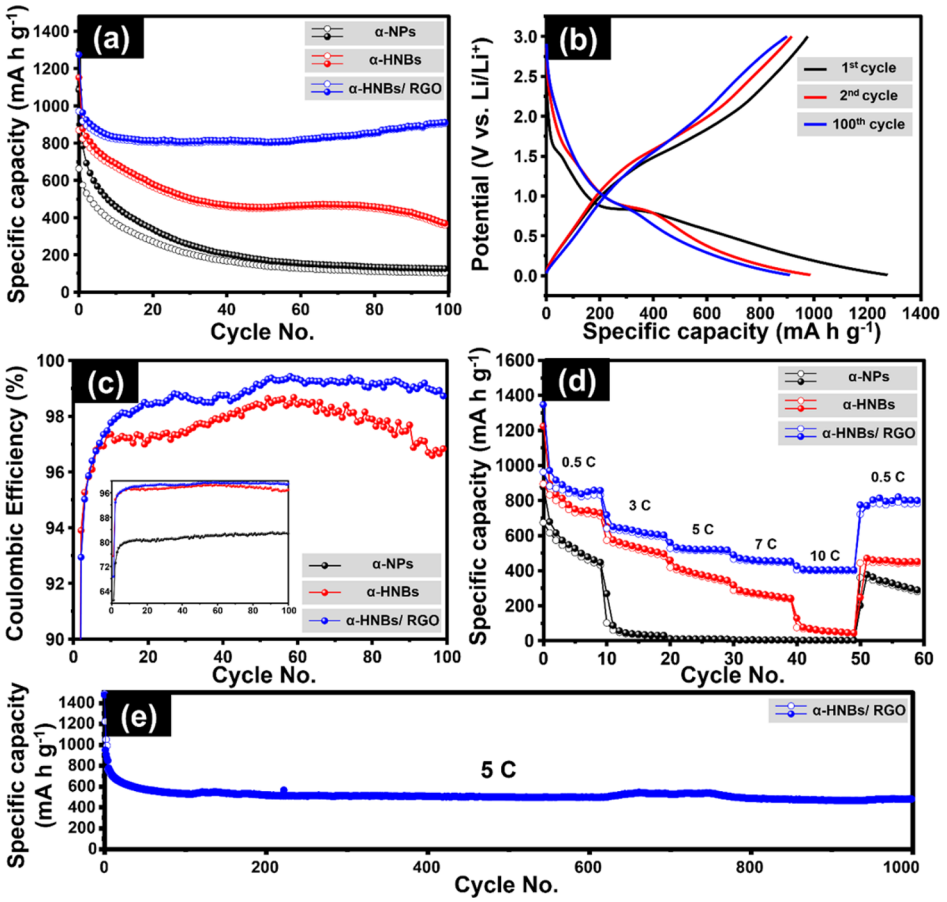

Figure 5. Electrochemical performance of α-NPs, α-HNBs, and α-HNBs/RGO: (a) Cyclability of specific capacity vs cycle number between 0.01 and 3 V at a current density of 0.5 C (500 mA g^{-1}); (b) charge/discharge curves of the α-HNBs/RGO electrode after various cycles; (c) Coulombic efficiency of α-NPs, α-HNBs, and α-HNBs/RGO; (d) rate capability of α-NPs, α-HNBs, and α-HNBs/RGO at various current densities (0.5, 3, 5, 7, 10, and 0.5 C); (e) long-term cycling of the α-HNBs/RGO at a current density of 5 C for 1000 cycles. The specific capacities are calculated by total mass of the nanocomposite.

g^{-1} at 0.5 C to 1 mA h g^{-1} at 10 C (retention: 62%; 0.5−0.5 C at last cycle), as reported in Table S3. By contrast, the α-HNBs electrode exhibited a more stable cyclic performance than the α-NPs at high current rates and delivered capacities of 727, 495, 344, 241, 44, and 470 mA h g^{-1} at 0.5, 3, 5, 7, 10, and 0.5 C, respectively, (retention: 64%; 0.5−0.5 C at last cycle), as shown in Table S3. The α-HNBs were expected to provide a higher rate capability at high rate than the α-NPs because of their structural integrity and short diffusion length. The capacity retentions of α-NPs and α-HNBs at 0.5 C show similar retention. However, the capacity of the α-NPs dramatically dropped beyond 3 C (19 mA h g^{-1}). The lower capacity retention and irreversible capacity can be distinctly attributed to the volume expansion of α-Fe_2O_3 and isolation from the current collectors, which cannot be involved in the electrochemical reaction with the Li^+ ion. Clearly, the α-HNBs/RGO electrode exhibits the highest capacity retention at all the current rates along with a better recovery of the capacity retention at the initial current rate of 0.5 C. The synergistic effect in α-HNBs/RGO provides structural integrity and excellent reversibility, which are attributed to the improved conductive network, electrical contacts induced by good bonding with the RGO functional groups, and high rate performance of α-HNBs offering a short diffusion path.

The morphology of the α-HNBs/RGO anode was further investigated to confirm the resistance of volume expansion induced by the unique structure of hollow nanobarrels, after insertion/extraction processes at a current density of 5 C. The ex situ observations by TEM elemental mapping (Figure 6) showed that the α-HNBs/RGO exists with carbon (RGO and EC/DEC), fluorine ($LiPF_6$), and iron (hollow nanobarrels) after the cycling test. It is confirmed that α-HNBs survived 50 cycles at a current density of 5 C without surface cracks and structural disintegration. These observations clearly explained the improved cyclability and rate capability during insertion/extraction.

To the best of our knowledge, these superior results show remarkable electrochemical performances compared to the performances of iron oxide previously reported in the literature. As shown in Figure 7, Fe_2O_3 with a graphene composite,[48] Fe_2O_3 nanorods,[25] nano-sized Fe_2O_3 with single-walled carbon nanotubes (CNTs),[30] Fe_2O_3 graphene composite,[49] graphene@Fe_2O_3 core−shells,[50] porous Fe_2O_3 nanorods N-doped RGO,[51] Fe_2O_3 nanoparticle with nanoribbons,[21] and Fe_2O_3 with RGO composite using microwave irradiation[52] were investigated with our α-HNBs/RGO electrode to compare the rate performances at various current densities. The α-HNBs/RGO electrode exhibits a small slope of the capacity drop, particularly for high current densities above 1000 and up to 10000 mA g^{-1}. Moreover, the discharge capacity at high current density shows the highest specific capacity and a good retention behavior, as shown in Table S4.

DOI: 10.1021/acsami.5b10342
ACS Appl. Mater. Interfaces 2016, 8, 2027−2034

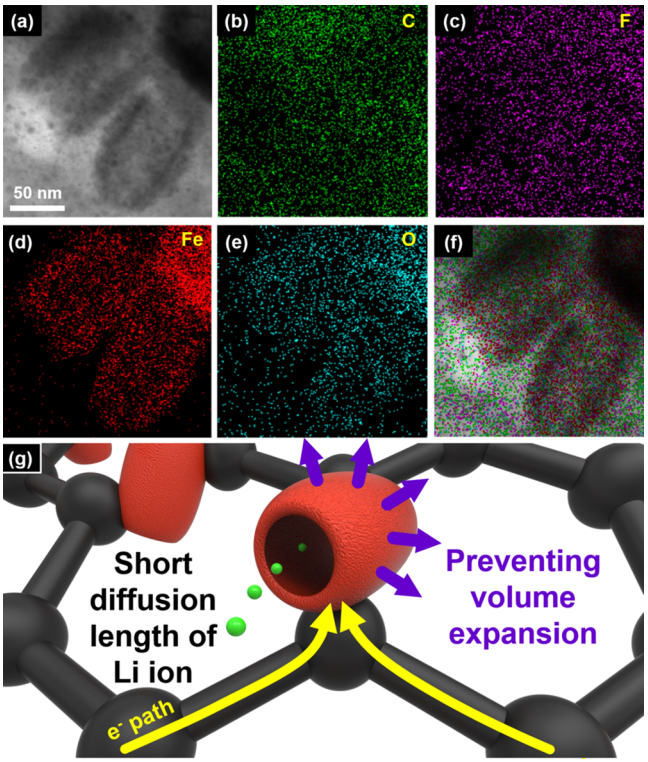

Figure 6. Elemental maps of the α-HNBs/RGO anode after 50 cycles at 5 C: (a) a bright-field TEM image; EDS mapping image of (b) carbon, (c) fluorine, (d) iron, and (e) oxygen, respectively; (f) an overlay of carbon, fluorine, iron, and oxygen maps. (g) Schematic illustration of structural advantages of the α-HNBs/RGO during insertion and extraction process.

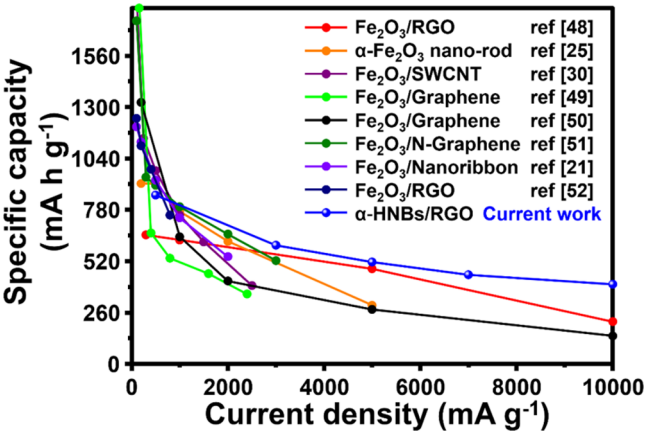

Figure 7. Comparison of the rate performance of the specific capacity vs current density of various Fe_2O_3-based anode materials for Li-ion batteries.

The electrochemical properties of the α-HNBs/RGO as an anode material were investigated by cyclic voltammetry (CV) at a scan rate of 0.1 mV s^{-1} for the first three cycles, as shown in Figure 8a. In the first scan, apparent cathodic peaks at 1.55 and 0.76 V were observed for the α-HNBs/RGO, which are attributed to the stepwise reduction of Fe^{3+} to Fe^{2+} and Fe^0, and the formation of the SEI layer, respectively.[27,30] Especially, the peak at ~0.76 V was ascribed to the lithiation of Fe_2O_3, according to the following reaction:[52,53]

$$Fe_2O_3 + 6Li^+ + 6e \leftrightarrow 2Fe + 3Li_2O$$

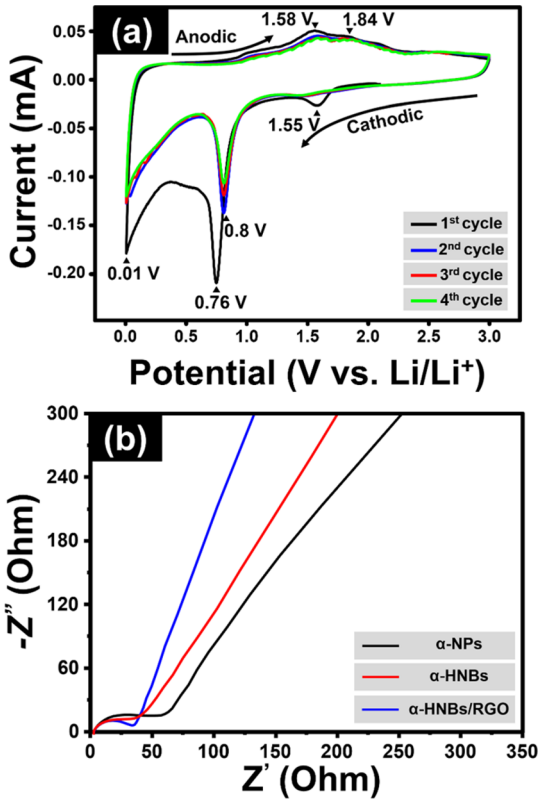

Figure 8. (a) Cyclic voltammetry curves of α-HNBs/RGO at a scan rate of 0.1 mV s^{-1} for four cycles. (b) Nyquist plots of α-NPs, α-HNBs, and α-HNBs/RGO from 4 MHz to 100 mHz.

On the other hand, the two peaks at 1.58 and 1.84 V in the first scan of the anodic step corresponded to the oxidation process of Fe^0 to Fe^{3+}.[30,39] However, the cathodic peak in the second cycle shows reducing or shifting of the peaks at 1.55, 0.76, and 0.01 V, as shown in the first cycle. This indicates that irreversible reactions were induced by the formation of an SEI layer on the electrode. During the subsequent cycles, the cathodic and anodic peaks were shifted from the first cycle because the formation of an SEI layer induced the electrode polarization.[11] The clearly interrupted electrolyte their time constants in the case of the LIBs are significantly similar.[54] Thus, in this study, the two R_{int} and R_{ct} components decomposition of the α-HNBs/RGO was confirmed by the CV results, which not only show well overlapped curves but also indicate a good reversibility of the Fe^0 to Fe^{3+} reaction.[30]

The Nyquist plot shows a depressed semicircle, which generally describes two components: charge transfer resistance (R_{ct})[55] and interfacial resistance (R_{int}: SEI resistance).[56] However, R_{ct} and R_{int} are difficult to separate, as were included in the total resistance, R_{tot}. Nyquist plots for all the specimens were measured from high to medium frequency at the open circuit potential, as shown in Figure 8b. The straight line in the low frequency region is the Warburg constant, which is assigned to the diffusion and transport of the Li^+ ion from the electrolyte to the surface of the electrode. The resistance of the depressed semicircle of α-HNBs/RGO (32 Ω) is lower than that of α-NPs (61 Ω) and α-HNBs (43 Ω). The steeper slope of α-HNBs/RGO indicates a faster diffusion kinetic of the Li^+ ion from the electrolyte to the electrode. These results can be explained by the Coulombic efficiency behavior.

DOI: 10.1021/acsami.5b10342
ACS Appl. Mater. Interfaces 2016, 8, 2027−2034

4. CONCLUSIONS

In summary, a one-step microwave-assisted hydrothermal method was used to fabricate an α-HNBs/RGO hybrid structure with a short reaction time, providing high stability and high capacity. Particularly, α-HNBs/RGO exhibited an enhanced electrochemical performance owing to the synergistic effect. The α-HNBs/RGO electrode had a high capacity of 916 mA h g^{-1} even after 100 cycles, and a high rate capability of 5000 mA h g^{-1} at a current density of 621 mA g^{-1}. The improved capacity, reversibility, Coulombic efficiency, rate capability (403 mA h g^{-1} at 10 C), and long-term cyclability (1000 cycles at 5 C) can be attributed to the synergistic effect between α-HNBs and RGO. The unique design of the anode has important effects, such as a better electrical conductivity, prevention of restacking of the RGO layer, and the formation of a 3D porous structure of RGO and hollowed α-Fe_2O_3, which offers buffer space to contain the severe volume expansion of iron oxide during the insertion/extraction reaction of the Li^+ ions. The α-HNBs/RGO composite appears promising as an advanced anode with a highly enhanced electrochemical performance, providing a long cycle life and high rate capability for high-performance energy storage systems.

■ ASSOCIATED CONTENT

Supporting Information

The Supporting Information is available free of charge on the ACS Publications website at DOI: 10.1021/acsami.5b10342.

Experimental details of synthesis of α-HNBs/RGO composite, TEM images, digital camera images, TGA curves, N_2 adsorption/desorption isotherms, rate capability, and tables (PDF)

■ AUTHOR INFORMATION

Corresponding Authors

*E-mail: wooyoung@yonsei.ac.kr. Tel: +82-2-2123-2834 (W.L.).

*E-mail: benedicto@gachon.ac.kr. Tel: +82-31-759-7015 (Y.S.Y.).

Notes

The authors declare no competing financial interest.

■ ACKNOWLEDGMENTS

This work was supported by the Ministry of Trade, Industry & Energy of the Korean government under Grant 20141510400050 of the Innovations in Nuclear Power Technology of the Korea Institute of Energy Technology Evaluation and Planning.

■ ABBREVIATIONS

(α-NPs), alpha-phase iron oxide nanoparticles
(α-HNBs), α-iron oxide hollow nanobarrels
(α-HNBs/RGO), α-HNBs on reduced graphene oxide

■ REFERENCES

(1) Armand, M.; Tarascon, J. M. Building Better Batteries. *Nature* **2008**, *451*, 652−657.

(2) Whittingham, M. S. Lithium Batteries and Cathode Materials. *Chem. Rev.* **2004**, *104*, 4271−4302.

(3) Liang, J.; Hu, H.; Park, H.; Xiao, C.; Ding, S.; Paik, U.; Lou, X. W. Construction of Hybrid Bowl-Like Structures by Anchoring Nio Nanosheets on Flat Carbon Hollow Particles with Enhanced Lithium Storage Properties. Energy Environ. *Energy Environ. Sci.* **2015**, *8*, 1707−1711.

(4) Hu, H.; Yu, L.; Gao, X.; Lin, Z.; Lou, X. W. Hierarchical Tubular Structures Constructed from Ultrathin TiO_2(B) Nanosheets for Highly Reversible Lithium Storage. *Energy Environ. Sci.* **2015**, *8*, 1480−1483.

(5) Ghadbeigi, L.; Harada, J. K.; Lettiere, B. R.; Sparks, T. D. Performance and Resource Considerations of Li-Ion Battery Electrode Materials. *Energy Environ. Sci.* **2015**, *8*, 1640−1650.

(6) Byeon, A.; Boota, M.; Beidaghi, M.; Aken, K. V.; Lee, J. W.; Gogotsi, Y. Effect of Hydrogenation on Performance of TiO_2(B) Nanowire for Lithium Ion Capacitors. *Electrochem. Commun.* **2015**, *60*, 199−203.

(7) Wu, Z.-S.; Zhou, G.; Yin, L.-C.; Ren, W.; Li, F.; Cheng, H.-M. Graphene/Metal Oxide Composite Electrode Materials for Energy Storage. *Nano Energy* **2012**, *1*, 107−131.

(8) Reddy, M. V.; Subba Rao, G. V.; Chowdari, B. V. R. Metal Oxides and Oxysalts as Anode Materials for Li Ion Batteries. *Chem. Rev.* **2013**, *113*, 5364−5457.

(9) Cai, D.; Lian, P.; Zhu, X.; Liang, S.; Yang, W.; Wang, H. High Specific Capacity of TiO2-Graphene Nanocomposite as an Anode Material for Lithium-Ion Batteries in an Enlarged Potential Window. *Electrochim. Acta* **2012**, *74*, 65−72.

(10) Tang, J.; Yang, J.; Zhou, L.; Xie, J.; Chen, G.; Zhou, X. Layer-by-Layer Self-Assembly of a Sandwich-Like Graphene Wrapped SnOx@ Graphene Composite as an Anode Material for Lithium Ion Batteries. *J. Mater. Chem. A* **2014**, *2*, 6292−6295.

(11) Kim, I. T.; Magasinski, A.; Jacob, K.; Yushin, G.; Tannenbaum, R. Synthesis and Electrochemical Performance of Reduced Graphene Oxide/Maghemite Composite Anode for Lithium Ion Batteries. *Carbon* **2013**, *52*, 56−64.

(12) Susantyoko, R. A.; Wang, X.; Xiao, Q.; Fitzgerald, E.; Zhang, Q. Sputtered Nickel Oxide on Vertically-Aligned Multiwall Carbon Nanotube Arrays for Lithium-Ion Batteries. *Carbon* **2014**, *68*, 619−627.

(13) Lee, J. M.; Hwang, H.-S.; Cho, W.-I.; Cho, B.-W.; Kim, K. Y. Effect of Silver Co-Sputtering on Amorphous V_2O_5 Thin-Films for Microbatteries. *J. Power Sources* **2004**, *136*, 122−131.

(14) Hou, C.; Lang, X. Y.; Han, G. F.; Li, Y. Q.; Zhao, L.; Wen, Z.; Zhu, Y. F.; Zhao, M.; Li, J. C.; Lian, J. S.; Jiang, Q. Integrated Solid/Nanoporous Copper/Oxide Hybrid Bulk Electrodes for High-Performance Lithium-Ion Batteries. *Sci. Rep.* **2013**, *3*, 2878.

(15) Wang, H.; Mao, N.; Shi, J.; Wang, Q.; Yu, W.; Wang, X. Cobalt Oxide-Carbon Nanosheet Nanoarchitecture as an Anode for High-Performance Lithium-Ion Battery. *ACS Appl. Mater. Interfaces* **2015**, *7*, 2882−2890.

(16) Ding, J.; Yan, X.; Li, J.; Shen, B.; Yang, J.; Chen, J.; Xue, Q. Enhancement of Field Emission and Photoluminescence Properties of Graphene-SnO_2 Composite Nanostructures. *ACS Appl. Mater. Interfaces* **2011**, *3*, 4299−305.

(17) Li, B.; Cao, H.; Zhang, J.; Qu, M.; Lian, F.; Kong, X. SnO_2−Carbon−Rgo Heterogeneous Electrode Materials with Enhanced Anode Performances in Lithium Ion Batteries. *J. Mater. Chem.* **2012**, *22*, 2851−2854.

(18) Zhang, F.; Cao, H.; Yue, D.; Zhang, J.; Qu, M. Enhanced Anode Performances of Polyaniline-TiO_2-Reduced Graphene Oxide Nanocomposites for Lithium Ion Batteries. *Inorg. Chem.* **2012**, *51*, 9544−9551.

(19) Li, X.; Huang, X.; Liu, D.; Wang, X.; Song, S.; Zhou, L.; Zhang, H. Synthesis of 3d Hierarchical Fe_3O_4/Graphene Composites with High Lithium Storage Capacity and for Controlled Drug Delivery. *J. Phys. Chem. C* **2011**, *115*, 21567−21573.

(20) Wu, Y.; Wei, Y.; Wang, J.; Jiang, K.; Fan, S. Conformal Fe_3O_4 Sheath on Aligned Carbon Nanotube Scaffolds as High-Performance Anodes for Lithium Ion Batteries. *Nano Lett.* **2013**, *13*, 818−823.

(21) Lin, J.; Raji, A.-R. O.; Nan, K.; Peng, Z.; Yan, Z.; Samuel, E. L. G.; Natelson, D.; Tour, J. M. Iron Oxide Nanoparticle and Graphene Nanoribbon Composite as an Anode Material for High-Performance Li-Ion Batteries. *Adv. Funct. Mater.* **2014**, *24*, 2044−2048.

DOI: 10.1021/acsami.5b10342
ACS Appl. Mater. Interfaces 2016, 8, 2027−2034

(22) Taberna, P. L.; Mitra, S.; Poizot, P.; Simon, P.; Tarascon, J. M. High Rate Capabilities Fe3o4-Based Cu Nano-Architectured Electrodes for Lithium-Ion Battery Applications. *Nat. Mater.* **2006**, *5*, 567−573.
(23) Chen, J. S.; Zhu, T.; Yang, X. H.; Yang, H. G.; Lou, X. W. Top-Down Fabrication of A-Fe_2O_3 Single-Crystal Nanodiscs and Microparticles with Tunable Porosity for Largely Improved Lithium Storage Properties. *J. Am. Chem. Soc.* **2010**, *132*, 13162−13164.
(24) Deng, H.-g.; Jin, S.-l.; Zhan, L.; Jin, M.-l.; Ling, L.-c. Morphology-Controlled Synthesis of Fe_3O_4/Carbon Nanostructures for Lithium Ion Batteries. *NEW CARBON MATER.* **2014**, *29*, 301−308.
(25) Lin, Y.-M.; Abel, P. R.; Heller, A.; Mullins, C. B. A-Fe_2O_3 Nanorods as Anode Material for Lithium Ion Batteries. *J. Phys. Chem. Lett.* **2011**, *2*, 2885−2891.
(26) Yang, Y.; Fan, X.; Casillas, G.; Peng, Z.; Ruan, G.; Wang, G.; Yacaman, M. J.; Tour, J. M. Three-Dimensional Nanoporous Fe_2O_3/Fe_3C-Graphene Heterogeneous Thin Films for Lithium-Ion Batteries. *ACS Nano* **2014**, *8*, 3939−3946.
(27) Zou, Y.; Kan, J.; Wang, Y. Fe_2O_3-Graphene Rice-on-Sheet Nanocomposite for High and Fast Lithium Ion Storage. *J. Phys. Chem. C* **2011**, *115*, 20747−20753.
(28) Yan, N.; Zhou, X.; Li, Y.; Wang, F.; Zhong, H.; Wang, H.; Chen, Q. Fe_2O_3 Nanoparticles Wrapped in Multi-Walled Carbon Nanotubes with Enhanced Lithium Storage Capability. *Sci. Rep.* **2013**, *3*, 3392.
(29) Lee, K. K.; Deng, S.; Fan, H. M.; Mhaisalkar, S.; Tan, H. R.; Tok, E. S.; Loh, K. P.; Chin, W. S.; Sow, C. H. Alpha-Fe_2O_3 Nanotubes-Reduced Graphene Oxide Composites as Synergistic Electrochemical Capacitor Materials. *Nanoscale* **2012**, *4*, 2958−2961.
(30) Zhou, G.; Wang, D.-W.; Hou, P.-X.; Li, W.; Li, N.; Liu, C.; Li, F.; Cheng, H.-M. A Nanosized Fe_2O_3 Decorated Single-Walled Carbon Nanotube Membrane as a High-Performance Flexible Anode for Lithium Ion Batteries. *J. Mater. Chem.* **2012**, *22*, 17942−17946.
(31) Boota, M.; Hatzell, K. B.; Alhabeb, M.; Kumbur, E. C.; Gogotsi, Y. Graphene-Containing Flowable Electrodes for Capacitive Energy Storage. *Carbon* **2015**, *92*, 142−149.
(32) Mazar Atabaki, M.; Kovacevic, R. Graphene Composites as Anode Materials in Lithium-Ion Batteries. *Electron. Mater. Lett.* **2013**, *9*, 133−153.
(33) Jia, C.-J.; Sun, L.-D.; Luo, F.; Han, X.-D.; Heyderman, L. J.; Yan, Z.-G.; Yan, C.-H.; Zheng, K.; Zhang, Z.; Takano, M.; Hayashi, N.; Eltschka, M.; Kläui, M.; Rüdiger, U.; Kasama, T.; Cervera-Gontard, L.; Dunin-Borkowski, R. E.; Tzvetkov, G.; Raabe, J. Large-Scale Synthesis of Single-Crystalline Iron Oxide Magnetic Nanorings. *J. Am. Chem. Soc.* **2008**, *130*, 16968−16977.
(34) Chen, D.; Li, L.; Guo, L. An Environment-Friendly Preparation of Reduced Graphene Oxide Nanosheets Via Amino Acid. *Nanotechnology* **2011**, *22*, 325601.
(35) Some, S.; Kim, Y.; Yoon, Y.; Yoo, H.; Lee, S.; Park, Y.; Lee, H. High-Quality Reduced Graphene Oxide by a Dual-Function Chemical Reduction and Healing Process. *Sci. Rep.* **2013**, *3*, 1929.
(36) Zhou, J.; Song, H.; Chen, X.; Zhi, L.; Yang, S.; Huo, J.; Yang, W. Carbon-Encapsulated Metal Oxide Hollow Nanoparticles and Metal Oxide Hollow Nanoparticles: A General Synthesis Strategy and Its Application to Lithium-Ion Batteries. *Chem. Mater.* **2009**, *21*, 2935−2940.
(37) Chen, Y.; Xia, H.; Lu, L.; Xue, J. Synthesis of Porous Hollow Fe_3O_4 Beads and Their Applications in Lithium Ion Batteries. *J. Mater. Chem.* **2012**, *22*, 5006−5012.
(38) Lee, S. H.; Yu, S. H.; Lee, J. E.; Jin, A.; Lee, D. J.; Lee, N.; Jo, H.; Shin, K.; Ahn, T. Y.; Kim, Y. W.; Choe, H.; Sung, Y. E.; Hyeon, T. Self-Assembled Fe_3O_4 Nanoparticle Clusters as High-Performance Anodes for Lithium Ion Batteries Via Geometric Confinement. *Nano Lett.* **2013**, *13*, 4249−4256.
(39) Luo, Y.; Luo, J.; Jiang, J.; Zhou, W.; Yang, H.; Qi, X.; Zhang, H.; Fan, H. J.; Yu, D. Y. W.; Li, C. M.; Yu, T. Seed-Assisted Synthesis of Highly Ordered TiO_2@A-Fe_2O_3 Core/Shell Arrays on Carbon Textiles for Lithium-Ion Battery Applications. *Energy Environ. Sci.* **2012**, *5*, 6559−6566.
(40) Fu, Y. Y.; Wang, R. M.; Xu, J.; Chen, J.; Yan, Y.; Narlikar, A. V.; Zhang, H. Synthesis of Large Arrays of Aligned A-Fe_2O_3 Nanowires. *Chem. Phys. Lett.* **2003**, *379*, 373−379.
(41) Stankovich, S.; Dikin, D. A.; Piner, R. D.; Kohlhaas, K. A.; Kleinhammes, A.; Jia, Y.; Wu, Y.; Nguyen, S. T.; Ruoff, R. S. Synthesis of Graphene-Based Nanosheets Via Chemical Reduction of Exfoliated Graphite Oxide. *Carbon* **2007**, *45*, 1558−1565.
(42) De Faria, D. L. A.; Venâncio Silva, S.; de Oliveira, M. T. Raman Microspectroscopy of Some Iron Oxides and Oxyhydroxides. *J. Raman Spectrosc.* **1997**, *28*, 873−878.
(43) Muraliganth, T.; Vadivel Murugan, A.; Manthiram, A. Facile Synthesis of Carbon-Decorated Single-Crystalline Fe_3O_4 Nanowires and Their Application as High Performance Anode in Lithium Ion Batteries. *Chem. Commun. (Cambridge, U. K.)* **2009**, 7360−7362.
(44) Zhou, J.; Song, H.; Ma, L.; Chen, X. Magnetite/Graphene Nanosheet Composites: Interfacial Interaction and Its Impact on the Durable High-Rate Performance in Lithium-Ion Batteries. *RSC Adv.* **2011**, *1*, 782−791.
(45) Wang, L.; Yu, Y.; Chen, P. C.; Zhang, D. W.; Chen, C. H. Electrospinning Synthesis of C/Fe_3O_4 Composite Nanofibers and Their Application for High Performance Lithium-Ion Batteries. *J. Power Sources* **2008**, *183*, 717−723.
(46) Poizot, P.; Laruelle, S.; Grugeon, S.; Dupont, L.; Tarascon, J.-M. Nano-Sized Transition-Metal Oxides as Negative-Electrode Materials for Lithium-Ion Batteries. *Nature* **2000**, *407*, 496−499.
(47) Pan, D.; Wang, S.; Zhao, B.; Wu, M.; Zhang, H.; Wang, Y.; Jiao, Z. Li Storage Properties of Disordered Graphene Nanosheets. *Chem. Mater.* **2009**, *21*, 3136−3142.
(48) Zhu, J.; Zhu, T.; Zhou, X.; Zhang, Y.; Lou, X. W.; Chen, X.; Zhang, H.; Hng, H. H.; Yan, Q. Facile Synthesis of Metal Oxide/Reduced Graphene Oxide Hybrids with High Lithium Storage Capacity and Stable Cyclability. *Nanoscale* **2011**, *3*, 1084−1089.
(49) Wang, G.; Liu, T.; Luo, Y.; Zhao, Y.; Ren, Z.; Bai, J.; Wang, H. Preparation of Fe2o3/Graphene Composite and Its Electrochemical Performance as an Anode Material for Lithium Ion Batteries. *J. Alloys Compd.* **2011**, *509*, L216−L220.
(50) Zhou, W.; Zhu, J.; Cheng, C.; Liu, J.; Yang, H.; Cong, C.; Guan, C.; Jia, X.; Fan, H. J.; Yan, Q.; Li, C. M.; Yu, T. A General Strategy toward Graphene@Metal Oxide Core-Shell Nanostructures for High-Performance Lithium Storage. *Energy Environ. Sci.* **2011**, *4*, 4954−4961.
(51) Hu, T.; Xie, M.; Zhong, J.; Sun, H.-t.; Sun, X.; Scott, S.; George, S. M.; Liu, C.-s.; Lian, J. Porous Fe_2O_3 Nanorods Anchored on Nitrogen-Doped Graphenes and Ultrathin Al_2O_3 Coating by Atomic Layer Deposition for Long-Lived Lithium Ion Battery Anode. *Carbon* **2014**, *76*, 141−147.
(52) Zhu, X.; Zhu, Y.; Murali, S.; Stoller, M. D.; Ruoff, R. S. Nanostructured Reduced Graphene Oxide/Fe_2O_3 Composite as a High-Performance Anode Material for Lithium Ion Batteries. *ACS Nano* **2011**, *5*, 3333−3338.
(53) Yuan, S.; Zhou, Z.; Li, G. Structural Evolution from Mesoporous α-Fe_2O_3 to Fe_3O_4@C and γ-Fe_2O_3 Nanospheres and Their Lithium Storage Performances. *CrystEngComm* **2011**, *13*, 4709−4713.
(54) Xu, K.; Zhang, S.; Jow, R. Electrochemical Impedance Study of Graphite/Electrolyte Interface Formed in Libob/Pc Electrolyte. *J. Power Sources* **2005**, *143*, 197−202.
(55) Chang, J.; Huang, X.; Zhou, G.; Cui, S.; Hallac, P. B.; Jiang, J.; Hurley, P. T.; Chen, J. Multilayered Si Nanoparticle/Reduced Graphene Oxide Hybrid as a High-Performance Lithium-Ion Battery Anode. *Adv. Mater.* **2014**, *26*, 758−764.
(56) Zhang, Y.; Wang, C.-Y.; Tang, X. Cycling Degradation of an Automotive $LiFePO_4$ Lithium-Ion Battery. *J. Power Sources* **2011**, *196*, 1513−1520.

DOI: 10.1021/acsami.5b10342
ACS Appl. Mater. Interfaces 2016, 8, 2027−2034